Short- and long-term gain dynamics in N_2^+ air lasing

Mathew Britton,[1] Marianna Lytova,[1] Patrick Laferrière,[1] Peng Peng,[1] Felipe Morales,[2] Dong Hyuk Ko,[1] Maria Richter,[2] Pavel Polynkin,[3] D. M. Villeneuve,[1,4] Chunmei Zhang,[1] Misha Ivanov,[2] Michael Spanner,[4] Ladan Arissian,[4,5] and P. B. Corkum[1,*]

[1]*Department of Physics, University of Ottawa, Ottawa K1N 6N5, Canada*
[2]*Max-Born Institute, Max-Born-Strasse 2A, Berlin D-12489, Germany*
[3]*College of Optical Sciences, The University of Arizona, Tucson, Arizona 85721, USA*
[4]*National Research Council of Canada, Ottawa K1A 0R6, Canada*
[5]*Center for High Technology Materials, Albuquerque, New Mexico 87106, USA*

Air lasing in the nitrogen molecular ion is not well understood because the complex physics responsible for gain is interwoven with pulse propagation in an extreme environment. Here we use a short gas jet to limit the interaction length, thereby removing the propagation effects. We report on several mechanisms that contribute to the decay of gain in different conditions, and experimentally isolate two decay timescales: the decay of long-term gain due to collisional state mixing, and short-term gain that cannot be explained by population inversion. To test the former, we control the inelastic electron scattering rate by varying the gas concentration while keeping the propagation length fixed, and predict the change of the decay using a model of collisional state mixing. We show that the same mechanism causes the decay of rotational wave packets in the states of the ion. Finally, we simulate the complex modulations of gain due to rotational wave packets and the propagation of the probe pulse through the evolving rotationally excited and inverted medium.

I. INTRODUCTION

Femtosecond laser pulses focused into air result in laser action in the ultraviolet, which is the so-called air laser [1]. Lasing can occur both from neutral nitrogen molecules and the nitrogen molecular cation N_2^+ [1,2]. In the case of N_2^+, emission occurs between the $B^2\Sigma_u^+$ and $X^2\Sigma_g^+$ electronic states. The emission can occur between various vibrational levels of both states. Air lasing can be initiated at a large distance in laser-produced filaments [3], leading to the possibility of a remote laser which is of interest in defense and remote sensing applications. Air lasing in N_2^+ has been demonstrated under a wide range of experimental conditions, but the mechanisms involved are still unclear [1,4–10]. A complete understanding of gain dynamics in N_2^+ will expand knowledge of strong field light-matter interactions and allow us to optimize control of air lasing. The current lack of understanding and consensus is unusual, as the interaction of N_2 with intense infrared light has been studied extensively in controlled environments.

Many of the processes that occur during air lasing in N_2 also occur during high-harmonic generation (HHG) [11]. An intense infrared pulse irradiating isolated N_2 can create a rotational wave packet that is composed of coherently prepared rotational eigenstates in an impulsive alignment process [12]. At higher laser intensities, field ionization becomes significant near $\sim$3 V Å^{-1}. In aligned nitrogen, the ionization probability increases by a factor of about 4 if the field is aligned parallel

instead of perpendicular to the molecular axis [13]. If the molecules are ionized, they are transferred predominantly to the $X^2\Sigma_g^+$ ground state of the ion [14]. A few percent of the ionization events create ions in the $B^2\Sigma_u^+$ excited state [15].

The most prominent difference between air lasing and HHG is that, in air lasing, the intense pump pulse continues to interact with the newly created ions after the harmonics are emitted. The pump pulse cycles population between the $X^2\Sigma_g^+$, $A^2\Pi_u$, and $B^2\Sigma_u^+$ states and adds further rotational and vibrational energy [16]. Thus, what we learn from air lasing in N_2^+ is important for understanding strong field interactions with simple quantum systems; it provides insight to more complex processes that underlie laser ionization mass spectrometry [17], optimal control of photochemical dissociation [18], and strong field interaction with solids [19].

Most experiments on N_2^+ laser gain are conducted in long gas media in which the intense laser pulse modifies the optical properties of the medium, leading to self-focusing, filamentation, and the creation of long plasma channels. The complex propagation process is accompanied by the spectral, temporal, and spatial reshaping of the pump pulse [3,20], which leads to uncontrolled pumping conditions and possible self-probing (or self-seeding) of gain.

In our experiment, we overcome this problem by restricting the propagation distance by using a gas jet in vacuum. The medium length is less than 1 mm, so that self-focusing and filamentation do not occur. This gives us more control over experimental conditions that we use in this paper to understand gain dynamics. We first develop and test a model to explain the decay of gain, and then we show that the decay
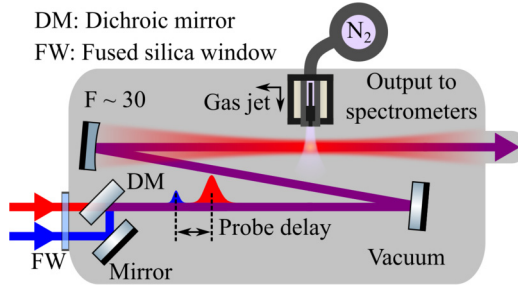
---

*pcorkum@uottawa.ca

FIG. 1. Experimental setup. A beam splitter separates the probe pulse from the pump pulse before the vacuum chamber. The probe pulse is frequency doubled to 400 nm and delayed. The probe pulse polarization is linear and rotated to be parallel to the linearly polarized pump pulse. After focusing, the emitted spectrum is sampled by an extreme ultraviolet spectrometer in vacuum or a UV/Vis fiber spectrometer in air.

of gain is related to the decay of rotational wave packets. While this long-term gain is similar to gain reported in air and using a gas cell [4,6,10,21–24], we also measure unusual short-term gain that exists within a few hundred femtoseconds of the pump pulse. To highlight the complex effects that cause the modulations in gain, we present simulations of the modulations obtained by propagating the probe pulse through the evolving rotationally excited and inverted medium.

II. EXPERIMENTAL DETAILS

In order to neglect the propagation effects, we minimize the interaction length by using a narrow supersonic gas jet in vacuum, as shown in Fig. 1. A 200-μm-wide pulsed valve with a ~5 bar backing pressure produces the nitrogen gas jet [25]. The nozzle geometry and experimental conditions prevent significant formation of clusters in the expanding jet [26]. Three linear stages control the position of the nozzle in three dimensions. We typically place the nozzle ~250 μm upstream from the laser focus. The pump pulse (~800 nm, ~32 fs, <2.5 mJ, f/30) is preserved after ionization without the effects of self-phase modulation and self-steepening, so the interaction is uniform and controlled. As expected, the pump spectrum does not broaden and self-seeding does not occur.

We use a weak second-harmonic probe pulse to observe amplification from N_2^+ at 391 nm [$B^2\Sigma_u^+$ ($\nu = 0$) $\rightarrow X^2\Sigma_g^+$ ($\nu = 0$)] and 428 nm [$B^2\Sigma_u^+$ ($\nu = 0$) $\rightarrow X^2\Sigma_g^+$ ($\nu = 1$)]. The polarizations of the pump and probe pulses are both linear and parallel to each other. We measure the probe spectrum after focusing using an ultraviolet-visible (UV/Vis) fiber spectrometer, and control the probe delay to resolve the gain dynamics. The measured bandwidth in our experiment is limited by the resolution of the fiber spectrometer (~0.5 nm), but the actual amplified spectrum is composed of a series of narrow emission lines. This signifies a complex emission in time that lasts for picoseconds after the probe pulse [10,22,27–29].

We integrate over a region of the amplified probe spectrum [$S(t)$] as a function of pump-probe time delay t, and divide by the average integrated intensity before zero delay (S_0) to obtain the amplification factor [$A(t) = \frac{S(t)}{S_0}$]. This method

produces a lower amplification factor because it averages over a spectral region. We choose a spectral region that includes the most prominent peak, which corresponds to the P branch. Alternatively, it is possible to fit the probe spectrum background and amplified peak to obtain the amplification factor, but the fitting model and parameters must be chosen carefully. We present our results as $gL = \ln[A(t)]$, where g is the gain coefficient and L is the length of the plasma channel in the gas jet. In typical conditions, gain is large ($gL \approx 1$ where $L \approx 500\,\mu$m).

We also measure high harmonics generated by the pump pulse using an inline extreme ultraviolet spectrometer. The cutoff in the HHG spectra provides a reliable and convenient measurement of the pump pulse intensity. The maximum intensity of the pump pulse at the focus is 8×10^{14} W cm^{-2} (f number ~30), but we use a half-wave plate and polarizer to attenuate it without changing the beam size. Another half-wave plate and polarizer attenuate the probe pulse. We observe that gain scales linearly with probe intensity, so the probe pulse measures the small-signal gain. We estimate the maximum intensity of the probe pulse to be 1×10^{10} W cm^{-2} using the calibrated pump pulse intensity and the relative energy, pulse duration, and focal spot size of the probe pulse.

III. RESULTS AND DISCUSSION

We measure gain dynamics that strongly depend on the position of the focus relative to the nozzle. Figure 2 shows the gain-length product (gL) as a function of probe delay at four positions along the gas flow direction in the expanding jet. In Fig. 2, x_0 refers to the closest position without obstructing the laser and $x_0 + 750\,\mu$m is the farthest position (and greatest gas expansion). Based on the focusing geometry and nozzle dimensions, x_0 is a few hundred microns. There are two prominent features that change with the expansion of the jet: deep modulations at rotational revivals and an overall decay. We first show that the decay is slower after expansion due to lower N_2^+ and electron density. Then, we discuss the prominent modulations that are due to rotational wave packets on the $X^2\Sigma_g^+$ and $B^2\Sigma_u^+$ states. Finally, we present results where we transition from long-term gain to unusual short-term gain.

A. Long-term gain

The timescale of the gain decay in Fig. 2 is expected for collisional state mixing. The lifetime of a transition in a plasma can be limited by inelastic scattering. In this case, the time required for inelastic scattering to equalize population in the $X^2\Sigma_g^+$ and $B^2\Sigma_u^+$ states of N_2^+ is important. The gain lifetime based on these inelastic collisions is $\tau \approx (\sigma \upsilon N)^{-1}$, where σ is the energy-dependent cross section that peaks at ~3×10^{-16} cm^{-2} for ~3.2 eV electrons [30] and N is the density of electrons or ions. We assume an initial plasma temperature of 5 eV, or an average electron speed of $\upsilon \approx 9 \times 10^5$ ms^{-1}. We measured the density in a similar jet to be $N \approx 2.5 \times 10^{18}$ cm^{-3} using single photon absorption.

For these conditions, the estimated gain lifetime of $\tau \approx$ 15 ps is consistent with the decay time observed in Fig. 2. For example, we obtained an exponential time constant of 18 ps by
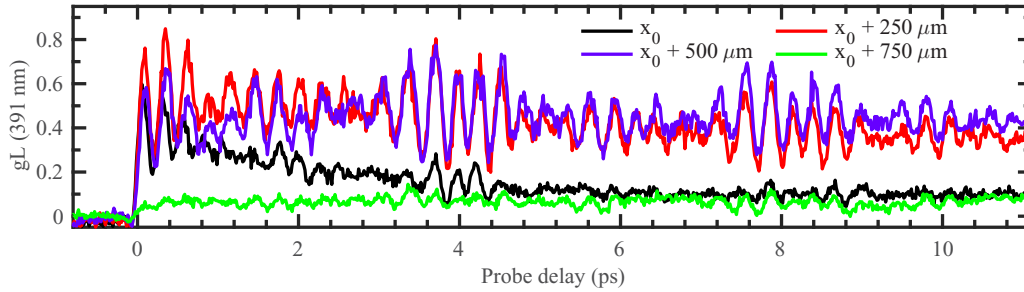
FIG. 2. Measured gain-length product gL of the 391 nm line as a function of pump-probe time delay. Each curve represents a measurement taken with the laser focused into the gas jet at a different distance from the nozzle in the direction of the gas expansion. x_0 represents the nearest possible position to the nozzle before the nozzle obstructs the laser. Expansion cooling creates a narrower initial rotational population distribution in both states that leads to longer rotational revivals and gain modulations. $I_{\text{pump}} = 4 \times 10^{14}$ W cm^{-2}.

fitting an exponential decay function to the curve corresponding to the position $x_0 + 250$ μm. A rigorous calculation will estimate the initial temperature by above-threshold ionization and rapid electron thermalization to a Maxwell-Boltzmann distribution. The population dynamics can then be rigorously determined from the measured cross section and the electron velocity distribution.

If the gain lifetime is indeed dictated by collisions, then the lifetime should increase as the gas density is decreased. To test this, we diluted the nitrogen gas in helium to reduce the density in a controlled way. We kept the position of the focus relative to the nozzle fixed at about $x_0 + 125$ μm. Figure 3 shows the effect of mixing helium with nitrogen while maintaining the same backing pressure on the jet. Helium has a higher ionization potential, which makes it difficult to ionize at these intensities. As a result, the electron and N$_2^+$ ion density scale with the partial pressure of N$_2$. In addition, helium is a rare gas and has no low-lying electronic states, so it contributes weakly to plasma cooling and thermalization. In contrast, the nonionized background molecules in air lasing serve as a heat sink for the electron energy.

Figure 3 shows that, when the N$_2$ density is reduced, gain is reduced and the decay is slower, as expected. We fit an exponential decay function to each curve in Fig. 3 to extract the decay rate with uncertainty. Figure 4 shows that the decay rate scales linearly with concentration. The picosecond timescale of the decay agrees with the estimated gain lifetime. These observations support the conclusion that electron-ion collisional deexcitation is responsible for the decay of gain [22,31]. It is also apparent from Fig. 3 that gain does not scale

linearly with density, which is unexpected. Usually, gain is proportional to the number of inverted atoms or molecules in the medium. In this case, gain scales quadratically with density [28].

In filamentation, the initial electron temperature is much lower and electron thermalization with other degrees of freedom is important due to the large heat capacity of nonionized molecules. The lower initial electron temperature will reduce the rate of collisional state mixing in air filaments [32]. The added energy exchange with neutral molecules will also change the electron temperature, and thus modify the rate. Therefore, in filaments we expect a slower decay compared to the gas jet. The slower decay should include another timescale arising from the redistribution of energy between the electrons and the vibrational and rotational degrees of freedom of neutrals.

B. Modulations

The structure and timing of the modulations are due to the rotational wave packets created by the pump pulse on the $X^2\Sigma_g^+$ and $B^2\Sigma_u^+$ states. These rotational wave packets modulate molecular alignment in the $X^2\Sigma_g^+$ or $B^2\Sigma_u^+$ state, which modulate absorption or gain, respectively. Figure 2 shows longer and deeper modulations at farther positions in the expanding jet. This is caused by expansion cooling in the jet that narrows the initial rotational population distribution in both states, which results in longer and deeper rotational revivals for gain modulation.
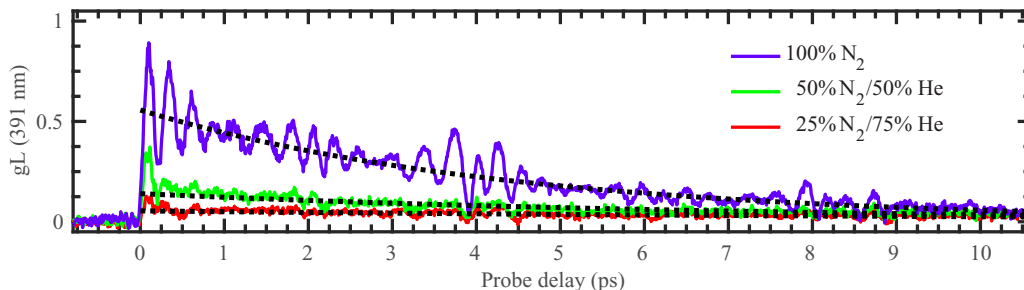

FIG. 3. Control of the decay rate using density. The densities of electrons and nitrogen ions scale with the partial pressure of nitrogen and influence gain and the decay rate. $I_{\text{pump}} = 3 \times 10^{14}$ W cm^{-2}.
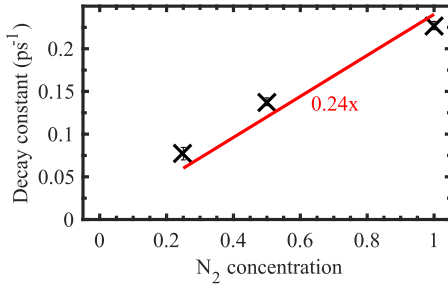
FIG. 4. The decay rate scales linearly with concentration. Lower density causes a proportionally slower decay. The uncertainties shown are from the fit only. $I_{pump} = 3 \times 10^{14}$ W cm^{-2}.

The transitions during collisional state mixing also make the rotational wave packets transfer from one state to the other. This random state mixing occurs over the same timescale as the decay of gain and contributes to decoherence of the rotational wave packets in both states. We observe this by fitting an exponential decay function to obtain the gain decay and then dividing by the gain decay fit. Figure 5(a) shows the amplitude of the modulations relative to the decay fit (gL/decay), which is constant over a timescale of several rotational periods. The modulations and gain decay together, as expected.

It is striking how much more complex the modulations are when compared with wave packets in HHG in N$_2$ [33]. This is because the wave packets encode details of the intense field interaction before, during, and after ionization. The wave packets are formed in the neutral molecule and then transferred to ionic states where additional rotational energy is added or withdrawn. Further complexity arises because the

transition moment favours orthogonal alignment between the $B^2\Sigma_u^+$ and $X^2\Sigma_g^+$ states, and the states evolve on different timescales due to slightly different rotational constants [34]. Finally, the probe pulse propagation through the rotating gain medium also adds complexity and must be considered.

To understand the modulations, we simulate rotational excitation by the pump and probe pulses in N$_2$ and N$_2^+$ and the probe pulse propagation through the evolving rotationally excited medium. The details of these simulations can be found in the Appendix and will be explored in greater detail in a future publication. Figure 5(b) shows the simulated gain modulations in the P branch for conditions similar to our experiment. The structure of the modulations depends on the input parameters, so agreement between experiment and simulation can be improved by adjusting the parameters. As in experiments, the simulated modulations are also complex compared to wave packets in HHG and they highlight the importance of the effects described above.

C. Short-term gain

In addition to the dynamics discussed so far, short-term gain appears for a few hundred femtoseconds after the pump and probe pulses are overlapped. Figure 6(a) shows the short-term gain in comparison with the long-term gain using different pump intensities. We isolate the short-term gain using low pump intensity, which diminishes the long-term gain.

Surprisingly, we observe short-term gain at two unusual transitions in some conditions: 420 nm [$B^2\Sigma_u^+$ ($v = 2$) $\rightarrow X^2\Sigma_g^+$($v = 3$)] and 424 nm [$B^2\Sigma_u^+$ ($v = 1$) $\rightarrow X^2\Sigma_g^+$($v = 2$)]. Figure 6(b) shows the short-term gain at three transitions simultaneously. Gain at
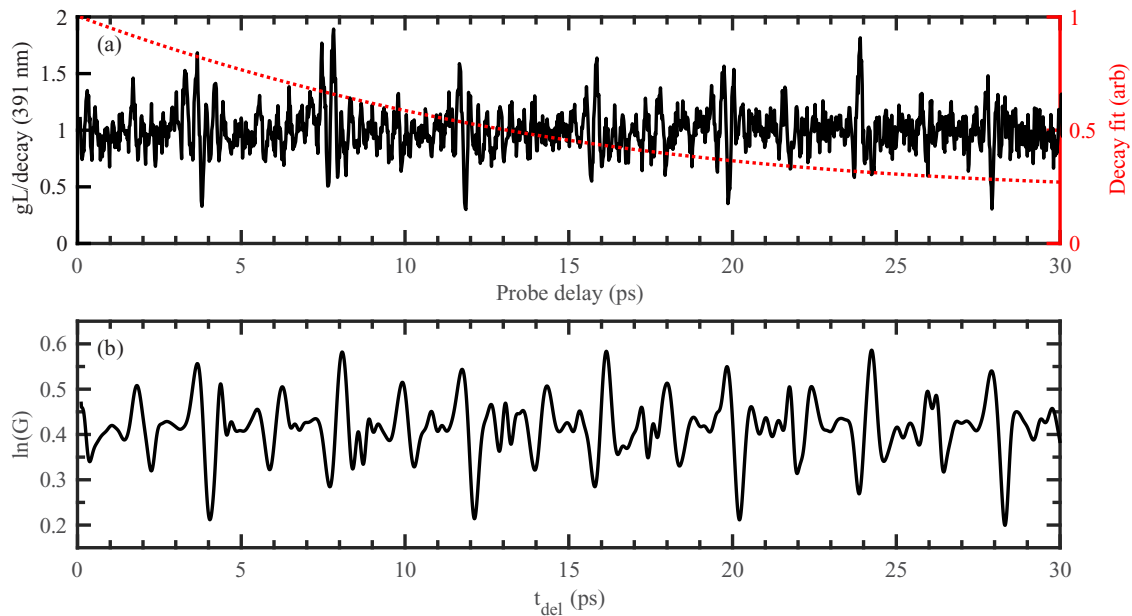

FIG. 5. (a) Gain-length product as a function of pump-probe delay time. The measured gL is factored into a decaying exponential part (red dashed line) and a quickly varying part. The quickly varying part is divided by the decaying exponential (black solid line). The modulations have a constant amplitude when the influence of the background decay is divided out. $I_{pump} = 2 \times 10^{14}$ W cm^{-2}. (b) Simulated gain in the P branch with complex modulations obtained by propagating a probe pulse through the inverted and rotationally excited N$_2^+$ medium. The simulation details can be found in the Appendix.
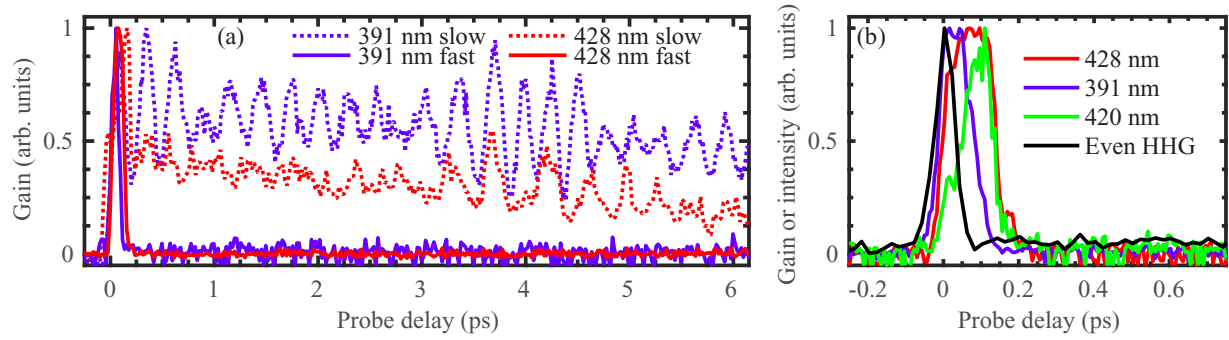
FIG. 6. (a) Two timescales of gain decay. Gain at 391 nm and 428 nm is normalized to the maximum value, showing long-term gain ("slow") and short-term gain ("fast") using different pump intensities and gas jet positions. (b) Short-term gain. The intensity of even high harmonics is also shown, indicating zero delay of the pump-probe overlap and the probe pulse duration. Short-term gain appears at unusual transitions, including 420 nm.

424 nm was also observed and behaves similarly to that at 420 nm. Gain on these unusual transitions was reported but not discussed in at least one prior publication [35].

The response time of even-order high-harmonics generated by the overlap of the pump pulse and second-harmonic probe pulse is also shown in Fig. 6(b). The even HHG signal indicates zero delay and the probe pulse duration. In comparison, the short-term gain on each transition continues to increase after the peak of the pump pulse has passed, and maximum gain occurs 20 to 100 fs after time overlap. Gain exists for about 200 fs, which is longer than the probe pulse duration.

We reduce the long-term gain compared to the short-term gain by lowering the intensity of both pump and probe pulses by moving the gas jet along the laser propagation direction. This effect is illustrated in Fig. 7 for the 428 nm emission. Moving the gas jet away from the focus along the laser propagation direction increases the laser spot size, which decreases the intensity. The intensity of the pump pulse decreases by a factor of $\sim$3.2 at $\sim$1.5z_R, and only the short-term gain remains. The long-term gain is significant at the focus, and the isolation of the short-term gain occurs symmetrically on both sides. We separately lowered the pump intensity by decreasing the pulse energy before the vacuum chamber to observe the same effect (not shown). We could not observe the effect by lowering the probe intensity.

The short-term gain has a few possible explanations. Gain is available for a few hundred femtoseconds, and collisional
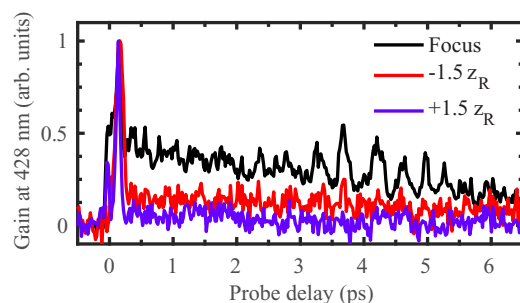

FIG. 7. Control of gain decay timescale using gas jet position. The gain at 428 nm is normalized to the maximum value, showing that the long-term gain changes to short-term gain at low intensity. The intensity is lowered by moving the gas jet along the laser propagation direction by $\sim$1.5z_R. $I_{\mathrm{pump}} = 2 \times 10^{14}$ W cm^{-2} (at focus).

state mixing occurs on the timescale of tens of picoseconds, so it cannot be the decay of population inversion. The rapid non-exponential decay of the short-term gain is also inconsistent with the decay of population. Recently, Miao *et al.* [36] observed similar short-term gain at 391 nm using a probe pulse spectrum that did not overlap 391 nm. Instead, they used an off-resonance probe pulse that overlapped another vibrational transition at 357 nm [$X^2\Sigma_g^+ (v = 0) \rightarrow B^2\Sigma_u^+ (v = 1)$]. They attribute short-term gain at 391 nm to vibrational Raman scattering enhanced by second-harmonic generated by the pump pulse, which then induces superfluorescence. Using an on-resonance probe pulse, they observed short-term gain in addition to relatively weak long-term gain, but they do not explain the on-resonance short-term gain.

In contrast, we measured purely short-term gain with an on-resonance probe pulse, and also tuned the significance of the long-term gain using the intensity of the pump pulse. The bandwidth of our probe pulse is broad enough to cover multiple vibrational transitions, so vibrational Raman scattering is possible; however, we observe simultaneous short-term gain at four transitions [e.g., Fig. 6(b) shows three]. This Raman scattering scheme cannot provide net amplification at all transitions within the bandwidth of pump and probe pulses.

In addition, we measure no second-harmonic signal generated by the pump pulse in the gas jet at typical intensities. At high intensities, the bandwidth of the second-harmonic generated by the pump pulse in the gas jet is much narrower than the probe pulse. Therefore, any Raman scattering in our measurements is due to the probe pulse alone and would not require time overlap between the pump and probe pulses. Without the requirement for time overlap, this mechanism does not explain the short-term gain. Our results require another explanation, which we will address in a future paper. One possibility is Raman gain in a *V*-type system involving the $X^2\Sigma_g^+$, $A^2\Pi_u$, and $B^2\Sigma_u^+$ states [37]. In this case, Raman gain on $B^2\Sigma_u^+$ to $X^2\Sigma_g^+$ transitions is accompanied by the absorption of pump photons on $X^2\Sigma_g^+$ to $A^2\Pi_u$ transitions.

IV. CONCLUSION

In conclusion, we used a supersonic gas jet to create a short medium that isolates air lasing from filamentation to

study N_2^+ gain in a two-color pump-probe configuration. We separated the short-term from the long-term gain by moving the gas jet along the laser propagation direction to lower the intensity. It would be hard to distinguish these two mechanisms in filamentation experiments where there is no control over pump-probe conditions.

We predicted the gain decay with a model of collisional state mixing and we confirmed the model by changing the density and gas composition to tune the rate of collisional state mixing. In the case of filamentation, where the initial electron temperature is lower and there is a large reservoir of neutral molecules, we expect a slower decay. The electron temperature and the rate of state mixing will change as energy is exchanged in these low-density neutral-dominated plasmas, which adds another timescale to the long-term gain.

We discussed complex modulations of gain due to rotational wave packets in the $X^2\Sigma_g^+$ and $B^2\Sigma_u^+$ states, and showed that collisional state mixing also causes the decay of these modulations. We presented simulations of the modulations that showed the influence of probe pulse propagation in the rotationally excited and inverted medium.

Now, with a confined medium that is reproducibly excited, we can introduce the powerful methods of femtosecond spectroscopy. In this case, the first intense pulse generates the ionized medium, the second (pump) pulse manipulates the medium, while the third (probe) pulse measures the amplification. This approach of separating ionization and pumping allows us to study the N_2^+ ion itself, instead of combining the first two steps using a single pump pulse. The additional pulse can test vibrational Raman scattering, control rotational wave packets, and mix electronic and vibrational population.

APPENDIX: SIMULATION DETAILS

We simulate the processes described above in two stages: pumping and probing. In our model, the pump is a strong (peak intensity $I_{p0} = 2 \times 10^{14}$ W cm^{-2}), short (duration $\tau_{on} = 64$ fs), nonresonant (wavelength $\lambda_p = 800$ nm, $\omega_p = 2\pi c/\lambda_p$) pulse:

$$E_p(t) = E_{p0}\cos(\omega_p t) \times \begin{cases} \sin(\pi t/\tau_{on}), & 0 \leqslant t < \tau_{on}, \\ 0, & t \geqslant \tau_{on}, \end{cases}$$
(A1)

which is assumed to be unchanged during the interaction. In addition, we further divide the pumping phase into two parts: before and after the peak. During the first half, we consider rotational pumping of the neutral component on vibrational

level $v = 0$ of the ground $X^1\Sigma_g^+$ state. At the peak of the pump pulse, we force ionization of the molecules and move some portion of the rotationally excited wave function to the $X^2\Sigma_g^+$ and $B^2\Sigma_u^+$ states of the ion, with an additional angle-dependent ionization probability roughly estimated as $P(\theta) = \cos^2\theta + \frac{1}{2}$ [38,39]. Here θ is the angle between the N_2 molecular axis and the electric field of the pump pulse. After the peak, we consider pumping not only for the neutral nitrogen, but also for the ionized molecules in the ground ($X^2\Sigma_g^+$) and excited ($B^2\Sigma_u^+$) states; again both refer to $v = 0$. Specifically, at the pumping stage, we solve a set of the Liouville–von Neumann quantum evolution equations for density matrices of the neutral molecular nitrogen $\hat\rho_N$ and molecular nitrogen cations $\hat\rho_X$, $\hat\rho_B$, that in atomic units (a.u.) are given by

$$i\partial_t\hat\rho_k^M(t) = [\hat H^M(t), \hat\rho_k^M(t)], \quad k = N, X, B, \quad \text{(A2)}$$

where index M refers to an azimuthal quantum number, and the time dependent Hamiltonian operator

$$\hat H^M(t) = B\hat{\mathbf{J}}^2 + \hat U_p^M(t) \quad \text{(A3)}$$

consists of the rotational operator (the same for all M) and the time-dependent interaction operator, respectively. In the case of all the mentioned Σ^+ states, eigenvectors of the rotational operator $B\hat{\mathbf{J}}^2$ are spherical harmonics $|JM\rangle$ [40], and the eigenenergies are

$$\mathcal{E}_J^{\text{Rot}} = \left(B_e - \frac{\beta_e}{2}\right)J(J+1) - D_e J^2(J+1)^2, \quad \text{(A4)}$$

where J is the rotational quantum number. For neutral nitrogen in the ground state $(B_e - \frac{\beta_e}{2}) = 1.989\,581$ cm^{-1}, $D_e = 5.76 \times 10^{-6}$ cm^{-1} [41]; whereas for molecular cations in the ground state (all in cm^{-1}) $B_e = 1.931\,76$, $\beta_e = 0.018\,81$, $D_e = 6.1 \times 10^{-6}$; and in the excited state $B_e = 2.07456$, $\beta_e = 0.024$, $D_e = 6.17 \times 10^{-6}$ [42]. The interaction potential between the polarizable molecule or cation and the oscillating linearly polarized field of the pump is given by

$$U_p(t) = -\tfrac{1}{2}(\alpha_\perp + \Delta\alpha\cos^2\theta)E_p^2(t), \quad \text{(A5)}$$

where the difference $\Delta\alpha = \alpha_\parallel - \alpha_\perp$ is expressed through the dominant elements of the polarizability tensor: $\alpha_\parallel$ and $\alpha_\perp$ [43]. We have calculated the required polarizabilities using the GAMESS electronic structure package [44], with the aug-cc-pVTZ basis set at a complete active space (CAS) multiconfigurational self-consistent field (MCSCF) level of theory, evaluated at the equilibrium bond length of the neutral molecule. For neutral molecular nitrogen we obtain $\Delta\alpha^N = 4.266$ a.u., $\alpha_\perp^N = 9.252$ a.u.; whereas, in case of N_2^+, $\Delta\alpha^X = 9.695$ a.u., $\alpha_\perp^X = 8.509$ a.u. and $\Delta\alpha^B = -4.68$ a.u., $\alpha_\perp^B = 6.582$ a.u.

All matrices in Eq. (A2) are of size $(J_{\max} + 1) \times (J_{\max} + 1)$, whereas the azimuthal quantum numbers $M = 0, \pm1, \ldots, \pm J_{\max 0}$. Here $J_{\max 0}$ is the maximum significant rotational number represented in the initial distribution for molecular nitrogen, which is assumed to be thermal. In particular, in our current computations for temperature $T = 50$ K, we estimate $J_{\max 0} = 14$. To take into account the process of Raman excitation admitting $\Delta J = \pm2$, we included in our consideration rotational numbers J up to $J_{\max} = 20 > J_{\max 0}$. Also we recall that the azimuthal quantum numbers M cannot be changed during the pumping due to the cylindrical symmetry of $U_p(t)$. As we stated before, in the case of $k =$

X, B we start solving (A2) only with $t = \tau_{on}/2$, so that the corresponding initial conditions are defined by (i) the angle-dependent ionization of the pumped neutral component, (ii) the nuclear spin statistic of the both electronic states, and (iii) the relative fraction of the ions in the ground, p_X, and excited $p_B = 1 - p_X$ states just after ionization. In our simulations, we set by hand $p_X = 0.15$, which corresponds to electronic inversion between $X^2\Sigma_g^+$ and $B^2\Sigma_u^+$.

Having calculated the density matrices, we compute the time-dependent refractive index of the medium caused by the rotational excitation:

$$
\begin{aligned}
n^2(t) = 1 &+ 4\pi N_{\text{mol}}[(1-\eta)\alpha_\perp^N + \eta p_X \alpha_\perp^X + \eta(1-p_X)\alpha_\perp^B \\
&+ (1-\eta)\Delta\alpha^N \langle \cos^2\theta \rangle_N(t) + \eta(p_X \Delta\alpha^X \langle \cos^2\theta \rangle_X(t) \\
&+ (1-p_X)\Delta\alpha^B \langle \cos^2\theta \rangle_B(t))],
\end{aligned}
\tag{A6}
$$

where $\langle \cos^2\theta \rangle_k$ are the measures of alignment [45] computed through the density matrices for each of the three components $k = N, X, B$. In our simulations, we also set by hand the molecular nitrogen density $N_{\text{mol}} = 5 \times 10^{18}$ cm^{-3} and overall degree of ionization $\eta = 0.1\%$.

To observe amplification at transitions between the pumped electronic states $B^2\Sigma_u^+$ and $X^2\Sigma_g^+$, the relatively weaker, $I_{s0} = 2 \times 10^{10}$ W cm^{-2}, resonant ($\lambda_0 = 400$ nm, $\omega_0 = 2\pi c/\lambda_0$) probe pulse is sent after the pump with some delay:

$$
E_s(t) = E_{s0} 2^{-\left(\frac{t-t_0}{\sigma_s/2}\right)^2} \cos[\omega_0(t-t_0)] \quad \text{at } z = 0 \tag{A7}
$$

where $\sigma_s = 25$ fs is the pulse width at the half-maximum and for definiteness we tie the position of maximum t_0 with delay time t_{del} in the following way: $t_0 = t_{\text{del}} + \sigma_s$. At the probing stage, we introduce a numerical model based on the simplified wave equation for the electric field of the probe pulse:

$$
\partial_t E_s(t,z) + c\partial_z E_s(t,z) = -2\pi \partial_t P(t,z), \tag{A8}
$$

subject to condition (A7) at $z = 0$. In Eq. (A8) the term on the right side describes the response of the medium and consists of three parts: (i) polarization due to the pumping, which is expressed through refractive index (A6), (ii) polarization caused by the seeded electronic transitions $B^2\Sigma_u^+ \leftrightarrows X^2\Sigma_g^+$, and (iii) polarization caused by the rotational excitation due to the probe pulse. To compute (ii) and (iii) for each space step in z, we need to solve the quantum evolution equation

$$
\mathrm{i}\partial_t \hat{\rho}^M(t,z) = [\hat{H}^M(t,z), \hat{\rho}^M(t,z)], \tag{A9}
$$

now with the Hamiltonian including the dipole operator for the electronic transitions:

$$
\hat{H}^M(t,z) = \hat{H}_0 + \hat{U}_s(t,z) - \hat{\mu}E_s(t,z)\cos\theta, \tag{A10}
$$

where the dipole moment $\mu_{XB} = -0.74$ a.u. is again computed using GAMESS at the equilibrium bond length of the neutral molecule. Note that, at the probing stage, all the matrices in (A9) are of size $(2J_{\max} + 1) \times (2J_{\max} + 1)$ and the initial condition for the density matrix is written in the block form as

$$
\rho^M(t_{\text{del}}) = \begin{bmatrix} \rho_X^M(t_{\text{del}}) & \varnothing \\ \varnothing & \rho_B^M(t_{\text{del}}) \end{bmatrix}, \tag{A11}
$$

where $\rho_X^M(t_{\text{del}})$ and $\rho_B^M(t_{\text{del}})$ are known from the computations performed during the pumping stage. Further, the unperturbed Hamiltonian in (A9) is given by

$$
\hat{H}_0 = \hat{H}_0^X + \hat{H}_0^B, \tag{A12}
$$

and we deal with the same eigenvectors as during the pumping stage:

$$
\hat{H}_0^X |X\rangle |JM\rangle = \mathcal{E}_J^{(X)} |X\rangle |JM\rangle, \tag{A13}
$$

$$
\hat{H}_0^B |B\rangle |JM\rangle = \mathcal{E}_J^{(B)} |B\rangle |JM\rangle, \tag{A14}
$$

which admit transitions with $\Delta J = \pm 1$ and $\Delta M = 0$. Now, eigenenergies for $v = 0$ are

$$
\mathcal{E}_J = T_e + \mathcal{E}_J^{\text{Rot}} + \frac{\omega_e}{2} - \frac{X_e\omega_e}{4} + \frac{Y_e\omega_e}{8}, \tag{A15}
$$

with the corresponding constants for the $X^2\Sigma_g^+$ state (in cm^{-1}) $T_e = 0$, $\omega_e = 2207.00$, $X_e\omega_e = 16.10$, $Y_e\omega_e = -0.040$; and for $B^2\Sigma_u^+$ state $T_e = 25461.4$, $\omega_e = 2419.84$, $X_e\omega_e = 23.18$, $Y_e\omega_e = -0.537$ [42].

Thus, at each step of the probe pulse propagation, both Eqs. (A8) and (A9) are solved one after another. At the final point $z_{\max} = 1$ mm, we compute the Fourier transform of the probe electric field to obtain the probe spectrum $I_{\text{out}}(\omega, t_{\text{del}})$ at the output, which depends on t_{del}. We are launching in parallel a set of thousands of probe pulses, whose time delays are stepped with 10 fs, so we can numerically calculate the emission gain through the spectral intensities as

$$
G(t_{\text{del}}) = 1 + \frac{\int_{\omega_{\min}}^{\omega_{\max}} [I_{\text{out}}(\omega, t_{\text{del}}) - I_{\text{in}}(\omega)]d\omega}{\int_{\omega_{\min}}^{\omega_{\max}} I_{\text{in}}(\omega)d\omega}, \tag{A16}
$$

where $[\omega_{\min}, \omega_{\max}]$ is the frequency region of interest, and $I_{\text{in}}(\omega)$ is spectrum of the input probe pulse. Further details about the numerical solution of the above equations will be outlined in an upcoming paper [46].

[1] J. Yao, B. Zeng, H. Xu, G. Li, W. Chu, J. Ni, H. Zhang, S. L. Chin, Y. Cheng, and Z. Xu, Phys. Rev. A **84**, 051802(R) (2011).

[2] D. Kartashov, S. Allšauskas, A. Baltuška, A. Schmitt-Sody, W. Roach, and P. Polynkin, Phys. Rev. A **88**, 041805(R) (2013).

[3] A. Couairon and A. Mysyrowicz, Phys. Rep. **441**, 47 (2007).

[4] Y. Liu, P. Ding, G. Lambert, A. Houard, V. Tikhonchuk, and A. Mysyrowicz, Phys. Rev. Lett. **115**, 133203 (2015).

[5] H. Xu, E. Lötstedt, A. Iwasaki, and K. Yamanouchi, Nat. Commun. **6**, 8347 (2015).

[6] M. Lei, C. Wu, A. Zhang, Q. Gong, and H. Jiang, Opt. Express **25**, 4535 (2017).

[7] Y. Liu, P. Ding, N. Ibrakovic, S. Bengtsson, S. Chen, R. Danylo, E. R. Simpson, E. W. Larsen, X. Zhang, Z. Fan, A. Houard, J. Mauritsson, A. L'Huillier, C. L. Arnold, S. Zhuang,

V. Tikhonchuk, and A. Mysyrowicz, Phys. Rev. Lett. **119**, 203205 (2017).

[8] M. Richter, F. Morales, M. Spanner, O. Smirnova, and M. Ivanov, in *2017 Conference on Lasers and Electro-Optics Europe European Quantum Electronics Conference (CLEO/Europe-EQEC)*, 25–29 June 2017, Munich (Optical Society of America, 2017), p. CG_P_15.

[9] A. Mysyrowicz, R. Danylo, P. Ding, A. Houard, V. Tikhonchuk, X. Zhang, Z. Fan, Q. Liang, S. Zhuang, L. Yuan, and Y. Liu, arXiv:1806.05818.

[10] L. Arissian, B. Kamer, A. Rastegari, D. M. Villeneuve, and J.-C. Diels, Phys. Rev. A **98**, 053438 (2018).

[11] P. B. Corkum, Phys. Rev. Lett. **71**, 1994 (1993).

[12] P. W. Dooley, I. V. Litvinyuk, K. F. Lee, D. M. Rayner, M. Spanner, D. M. Villeneuve, and P. B. Corkum, Phys. Rev. A **68**, 023406 (2003).

[13] Z. X. Zhao, X. M. Tong, and C. D. Lin, Phys. Rev. A **67**, 043404 (2003).

[14] J. Itatani, J. Levesque, D. Zeidler, H. Niikura, H. Pépin, J. C. Kieffer, P. B. Corkum, and D. M. Villeneuve, Nature (London) **432**, 867 (2004).

[15] I. V. Litvinyuk, F. Légaré, P. W. Dooley, D. M. Villeneuve, P. B. Corkum, J. Zanghellini, A. Pegarkov, C. Fabian, and T. Brabec, Phys. Rev. Lett. **94**, 033003 (2005).

[16] J. Yao, S. Jiang, W. Chu, B. Zeng, C. Wu, R. Lu, Z. Li, H. Xie, G. Li, C. Yu, Z. Wang, H. Jiang, Q. Gong, and Y. Cheng, Phys. Rev. Lett. **116**, 143007 (2016).

[17] J. Peng, N. Puskas, P. B. Corkum, D. M. Rayner, and A. V. Loboda, Anal. Chem. **84**, 5633 (2012).

[18] B. J. Sussman, D. Townsend, M. Y. Ivanov, and A. Stolow, Science **314**, 278 (2006).

[19] G. Vampa, T. J. Hammond, N. Thiré, B. E. Schmidt, F. Légaré, C. R. McDonald, T. Brabec, and P. B. Corkum, Nature (London) **522**, 462 (2015).

[20] L. Arissian, D. Mirell, S. Rostami, A. Bernstein, D. Faccio, and J.-C. Diels, Opt. Express **20**, 8337 (2012).

[21] B. Xu, S. Jiang, J. Yao, J. Chen, Z. Liu, W. Chu, Y. Wan, F. Zhang, L. Qiao, R. Lu, Y. Cheng, and Z. Xu, Opt. Express **26**, 13331 (2018).

[22] X. Zhong, Z. Miao, L. Zhang, H. Jiang, Y. Liu, Q. Gong, and C. Wu, Phys. Rev. A **97**, 033409 (2018).

[23] X. Zhong, Z. Miao, L. Zhang, Q. Liang, M. Lei, H. Jiang, Y. Liu, Q. Gong, and C. Wu, Phys. Rev. A **96**, 043422 (2017).

[24] H. Zhang, C. Jing, J. Yao, G. Li, B. Zeng, W. Chu, J. Ni, H. Xie, H. Xu, S. L. Chin, K. Yamanouchi, Y. Cheng, and Z. Xu, Phys. Rev. X **3**, 041009 (2013).

[25] M. Britton, P. Laferrière, D. H. Ko, Z. Li, F. Kong, G. Brown, A. Naumov, C. Zhang, L. Arissian, and P. B. Corkum, Phys. Rev. Lett. **120**, 133208 (2018).

[26] O. F. Hagena and W. Obert, J. Chem. Phys. **56**, 1793 (1972).

[27] A. Azarm, P. Corkum, and P. Polynkin, Phys. Rev. A **96**, 051401(R) (2017).

[28] G. Li, C. Jing, B. Zeng, H. Xie, J. Yao, W. Chu, J. Ni, H. Zhang, H. Xu, Y. Cheng, and Z. Xu, Phys. Rev. A **89**, 033833 (2014).

[29] J. Yao, G. Li, C. Jing, B. Zeng, W. Chu, J. Ni, H. Zhang, H. Xie, C. Zhang, H. Li, H. Xu, S. L. Chin, Y. Cheng, and Z. Xu, New J. Phys. **15**, 023046 (2013).

[30] O. Nagy, C. P. Ballance, K. A. Berrington, P. G. Burke, and B. M. McLaughlin, J. Phys. B: At. Mol. Opt. Phys. **32**, L469 (1999).

[31] M. Lei, C. Wu, Q. Liang, A. Zhang, Y. Li, Q. Cheng, S. Wang, H. Yang, Q. Gong, and H. Jiang, J. Phys. B: At. Mol. Opt. Phys. **50**, 145101 (2017).

[32] Z. Sun, J. Chen, and W. Rudolph, Phys. Rev. E **83**, 046408 (2011).

[33] J. Itatani, D. Zeidler, J. Levesque, M. Spanner, D. M. Villeneuve, and P. B. Corkum, Phys. Rev. Lett. **94**, 123902 (2005).

[34] D. Kartashov, S. Haessler, S. Ališauskas, G. Andriukaitis, A. Pugžlys, A. Baltuška, J. Möhring, D. Starukhin, M. Motzkus, A. Zheltikov, M. Richter, F. Morales, O. Smirnova, M. Y. Ivanov, and M. Spanner, in *Research in Optical Sciences* (Optical Society of America, Washington, 2014), p. HTh4B.5.

[35] J. Ni, W. Chu, H. Zhang, C. Jing, J. Yao, H. Xu, B. Zeng, G. Li, C. Zhang, S. L. Chin, Y. Cheng, and Z. Xu, Opt. Express **20**, 20970 (2012).

[36] Z. Miao, X. Zhong, L. Zhang, W. Zheng, Y. Gao, Y. Liu, H. Jiang, Q. Gong, and C. Wu, Phys. Rev. A **98**, 033402 (2018).

[37] V. V. Kozlov, P. G. Polynkin, and M. O. Scully, Phys. Rev. A **59**, 3060 (1999).

[38] D. Pavičić, K. F. Lee, D. M. Rayner, P. B. Corkum, and D. M. Villeneuve, Phys. Rev. Lett. **98**, 243001 (2007).

[39] M. Spanner and S. Patchkovskii, Chem. Phys. **414**, 10 (2013).

[40] R. Zare, *Angular Momentum* (Wiley-Interscience, New York, 1987).

[41] G. Herzberg, *Molecular Spectra and Molecular Structure: Volume I - Spectra of Diatomic Molecules*, 2nd ed. (Krieger, Malabar, FL, 1989).

[42] L. Klynning and P. Pagès, Phys. Scr. **25**, 543 (1982).

[43] R. Boyd, *Nonlinear Optics*, 3rd ed. (Elsevier, Amsterdam, 2008).

[44] M. Schmidt, K. Baldridge, J. Boatz, S. Elbert, M. Gordon, J. Jensen, S. Koseki, N. Matsunaga, K. Nguyen, S. Su, T. Windus, M. Dupuis, and J. Montgomery, Jr., J. Comput. Chem. **14**, 1347 (1993).

[45] B. Friedrich and D. Herschbach, Phys. Rev. Lett. **74**, 4623 (1995).

[46] M. Lytova, M. Richter, F. Morales, O. Smirnova, M. Ivanov, and M. Spanner (unpublished).